In-situ proton irradiation/lead-bismuth eutectic corrosion synergistic effect on amorphous FeCrAlTiMo coatings

Jian Yang[a], Jijun Yang[a,⎺]

[a] *Key Laboratory of Radiation Physics and Technology of Ministry of Education, Institute of Nuclear Science and Technology, Sichuan University, Chengdu,610064, China*
[b] *Laboratory of Science and Technology on Reactor Fuel and Materials, Nuclear Power Institute of China, Chengdu, Sichuan 610041, China*

Abstract

Synergistic effect of the simultaneous proton irradiation and lead-bismuth eutectic (LBE) corrosion on the amorphous FeCrAlTiMo coatings was investigated. Results displayed that proton irradiation had a positive effect on LBE corrosion resistance of the coating. The experimental and simulation results demonstrated that irradiation-induced annihilation of the free volume reduced the diffusion kinetic and lead to slower corrosion rate at 600 ℃, which challenged the traditional wisdom that irradiation damage resulted in negative effect on materials corrosion. Finally, a novel mechanism of irradiation-decelerated corrosion was proposed, which provided a new approach for designing nuclear-structural materials with better corrosion and irradiation resistance.

⎺ **Corresponding author:** jjyang@scu.edu.cn **(Jijun Yang)**

1. Introduction

Current Generation IV advanced nuclear energy systems put forward an extremely challenging operating environment, with higher temperature, stronger irradiation and more corrosive coolants [1]. Along with this, the compatibility problem of in-reactor structural materials and corrosive coolants has become one of the key bottlenecks restricting their development [2]. In recent years, various coolant corrosion and irradiation assisted corrosion are continued focus of concern for structural materials in advanced nuclear reactors [3, 4]. To accurately evaluate the service life of the in-reactor material component, a thorough understanding of the synergistic effect of simultaneous coolant corrosion and irradiation is critical.

To date, many post-irradiation corrosion and in situ-irradiation corrosion studies have been accumulated to elucidate the effects of irradiation on corrosion in various coolants, including liquid lead-bismuth eutectic (LBE) [5], molten salts [6], water-based environment [7], supercritical CO_2 [8] and more. Gradually, there is a consensus that irradiation accelerates the corrosion rate of structural materials in today's reactors. The mechanism of irradiation-accelerated corrosion can be generally attributed to two main aspects. It's well established that the displacement damage effects caused by irradiation can introduce a considerable number of vacancies and interstitials, which further evolve into dislocation lines/loops/walls, voids, bubbles and other defects through migration and merger. These defects can provide quick pathways for the movement of elements in the materials, increasing their diffusion rate and thus accelerating overall corrosion [9]. Besides, irradiation-enhanced diffusion also can induce spatial changes in the distribution of chemical composition within the materials, concretely manifested as phase transformation, precipitation, segregation, etc., which will especially promote the localized corrosion [10].

In fact, some experiments have also confirmed the existence of irradiation-decelerated corrosion, such as proton-irradiated Ni-Cr alloys in high-temperature molten salts [11] and Au^{2+}-irradiated FeCrAlTiMo coatings in high-temperature liquid LBE [12], indicating that multiple competitive mechanisms introduced by irradiation

co-affect corrosion. However, the explanation for this potential irradiation-decelerated corrosion mechanism have remained hidden. Obviously, from the perspective of long-term safe service of in-reactor structural materials, irradiation-accelerated corrosion is not expected. If one of the irradiation-decelerated corrosion mechanisms can be revealed, and some material systems adapted to these mechanisms can be designed and developed, it will greatly promote the development of advanced nuclear reactors.

Herein, based on the irradiation-accelerated corrosion mechanisms mentioned above, an amorphous FeCrAlTiMo high-entropy alloy (HEA) coating is specially designed and prepared. Subsequently, the synergistic effects of simultaneous proton irradiation and LBE corrosion are investigated. The results show that proton irradiation can decelerate corrosion of FeCrAlTiMo coating in LBE, contradicting irradiation-accelerated corrosion commonly reported. The deceleration is determined and quantified by cross-sectional TEM analysis, displaying the thickness of corrosion-induced oxide film. Combining experimental and simulation (molecular dynamics, MD) results, we propose an irradiation-decelerated corrosion mechanism, which is the result of irradiation-induced annihilation of the free volume in amorphous alloys and thus weakening the element diffusion. Moreover, our work also provides a new strategy for the design of innovative structural materials in future advanced nuclear reactors.

2. Methods

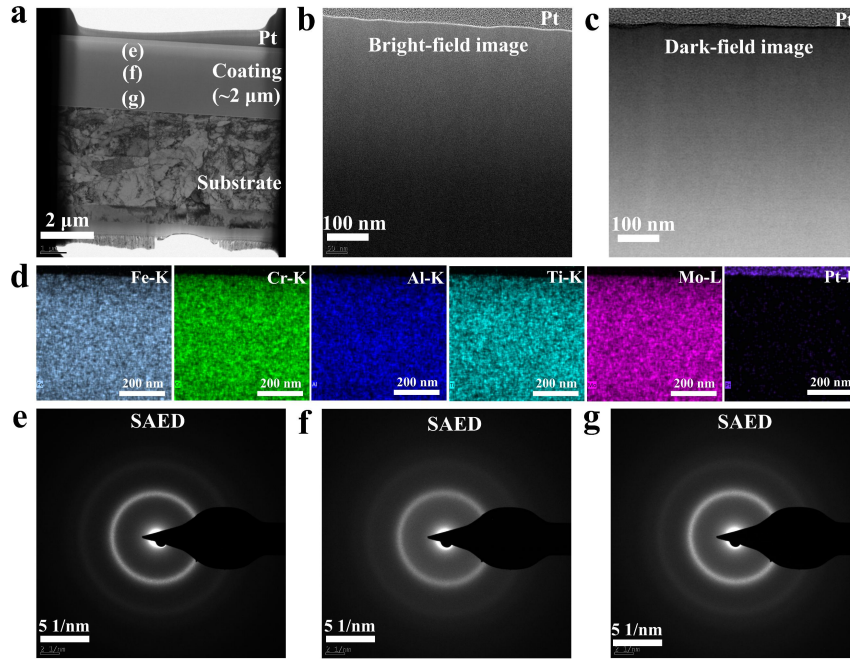### 2.1 Corrosion/irradiation sample fabrication

Fig. 1. Microstructure analysis of the pristine FeCrAlTiMo coating: **a** cross-sectional TEM image; **b** Bright-field and **c** dark-field TEM images of the coating; **d** EDS mapping of the coating; **e-g** Selected electron diffraction patterns of the areas of the coating, as marked in **a**.

We used magnetron sputtering as the fabrication method. The 12Cr2W1Mn F/M steel, designed especially for LFR, with a final machining thickness of about 80 μm and a shape of 10×10 mm^2 was selected as substrate, and a FeCrAlTiMo alloy target (99.99 wt.% purity) with equal molar ratio was used for coating sputtering. The background vacuum was 1×10^{-6} mbar. During deposition, the Ar working pressure was 5×10^{-4} mbar, the working temperature was 350 ℃, the sputtering power density was about 6.6 W/cm^2, substrate bias voltage was -100 V, target/substrate distance was 15 cm and the deposition rate was 20 nm/min. Before corrosion/irradiation tests, the microstructure of the pristine FeCrAlTiMo coating was identified by TEM, as shown in **Fig. 1**. Both the bright-field and dark-field TEM images were featureless, and no significant local color contrast was observed (**Fig. 1b-c**). The EDS mapping results showed that all components of the coating were uniformly distributed without any distinguishable element segregation or aggregation (**Fig. 1d**). Moreover, the SAED

patterns at different depths of the coating presented similar diffraction halos, corresponding to amorphous characteristics (**Fig. 1e-g**). These results all indicated that the pristine FeCrAlTiMo coating possessed a completely amorphous phase structure. The nominal composition of the coating was determined by EDS as Fe-22.2 at%, Cr-21.6 at%, Al-20.2 at%, Ti-16.1 at% and Mo-19.9 at%, and the coating thickness was about 2.0 μm, which was thin enough to allow most energetic protons to penetrate whole substrate/coating sample foil (~82 μm), proving that the corrosion/irradiation experiment was feasible and could be successfully achieved, as shown in **Fig. 2** and **Fig. 3**.
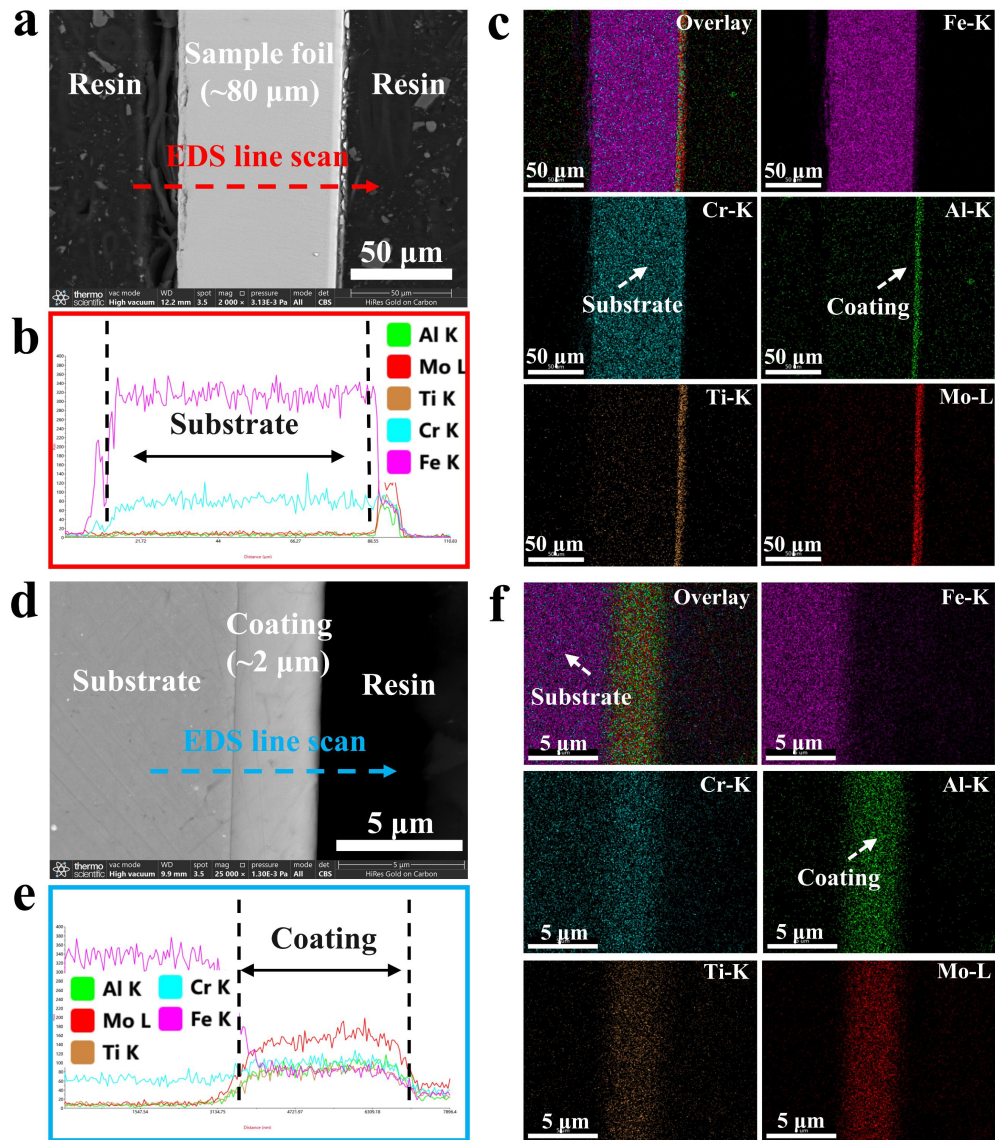

Fig. 2. The analysis of SEM morphology and element distribution of the sample foil (substrate + coating) used in corrosion/irradiation experiment. **a** SEM morphology image, **b** EDS line scan and

c EDS mapping of the sample foil; **d** SEM morphology image, **e** EDS line scan and **f** EDS mapping of the FeCrAlTiMo coating.

2.2 Corrosion/irradiation experiments

The simultaneous proton irradiation and LBE corrosion experiments were carried out based on the 3 MV tandem accelerator (HVEE, High Voltage Engineering Europa) of the Institute of Nuclear Science and Technology, Sichuan University, Chengdu, China. The details of the facility used in this study also could be referred to our previous research [13]. The substrate/coating sample foil was sandwiched between two graphite washers. The coated side was directly exposed to liquid LBE, and the proton beam was injected from the other side, so long as the protons could pass through the entire sample foil, the coating was irradiated and corroded simultaneously. Notably, the window that allowed the proton beam to shine onto the sample foil was 3 mm in diameter, and the hollow inner diameter of the graphite washer was 5 mm. In view of this, two typical areas were obtained on the coated side, one was "corrosion only" and the other was "corrosion plus irradiation". The synergistic effect of irradiation and corrosion was elucidated by comparing the corrosion behavior of the coating in the two areas. The sketch of this corrosion/irradiation experiment facility was shown in **Fig. 3a**.

After the pressure of accelerator vacuum chamber reached 1×10^{-7} mbar, the heater was started to heat up the corrosion cell to the target temperature (600 °C) over a period of roughly 1 h. Then the proton beam with a particle energy of 5.5 MeV was introduced into the sample, and the experiment officially began. During irradiation/corrosion, the proton beam flux was 5.6×10^{12} ions/(cm$^2\cdot$s) and the average beam current was 3.48 μA/cm^2. The total irradiation/corrosion time was 12 h, the total proton injection fluence was 2.0×10^{17} ions/cm^2 and the oxygen concentration in LBE was 3.6×10^{-3} wt.%. Once the targeted duration of the corrosion and proton injection fluence were reached, the proton beam was cut off and the heater was stopped, making the end of experiment.

2.3 Sample characterization

The microstructure of the coating and formed oxide film was characterized by a field-emission scanning electron microscope (FESEM, INSPECT F50, FEI) and a field emission transmission electron microscope (TEM, FEI Talos F200s super-X) equipped with an energy dispersive spectrometer equipped with an energy dispersive spectrometer (EDS). The TEM thin foils were prepared by a dual-beam Focused Ion Beam (FIB, Thermo Scientific Helios 5 CX) instrument lift-out from both the "corrosion only" and "corrosion plus irradiation" areas. Before FIB milling, a platinum (Pt) layer with a thickness of about 0.5 μm were deposited to protect the surface from the later Ga ions irradiation damage. These TEM foils were thinned gradually using 30 kV, 16 kV, 8 kV, 5kV and 2 kV Ga ions to ~1000 nm, ~500 nm, ~200 nm, ~100 nm and ~50 nm, respectively. The final milling voltage and current was 2 kV and 20 pA, respectively, which was sufficiently small to reduce the FIB damage. After the irradiation/corrosion experiment, the sample foil was immersed in a mixed solution of H_2O_2 (hydrogen peroxide), CH_3COOH (acetic acid) and CH_3CH_2OH (ethanol) with a volume ratio of 1:1:1 at room temperature to remove residual LBE on surface.

2.4 Molecular dynamic (MD) simulations

MD simulations were performed by Large-scale Atomic/Molecular Massively Parallel Simulator (LAMMPS) software package [14] to calculate the evolution of free volume of the coating and the variation of diffusion coefficient of coating components before and after irradiation. First, a simulation box, labeled FCATM (110), containing 75600 atoms with a BCC crystal structure was constructed, in which Fe, Cr, Al, Ti and Mo atoms were randomly distributed to occupy the lattice sites, as shown in **Fig. 8j**. The simulation used NPT ensemble and started from the crystalline structure FCATM (110) at 873.5 K (600 ℃). The system was heated to 5500 K during 400 ps, then isothermally equilibrated at NVE ensemble for 400 ps, and finally cooled

from 5500 K down to 873.5 K within 400 ps and isothermally equilibrated for another 400 ps. Eventually, the completely amorphous FeCrAlTiMo coating, labeled FCATM' (110), was obtained by structural analysis of OVITO software **(Fig. 8k)**.

The diffusion rates of each element before and after 5.5 MeV proton irradiation with a dose of 2.0×10^{17} ions/cm^2 on FCATM' (110) surface have been also calculated. The interatomic interactions between Fe, Cr, Al, Ti and Mo atoms in this work were described by embedded-atom method (EAM) potentials [15]. The EAM potentials were validated by comparing the formation energies of defects, equilibrium volumes, elastic moduli, and heat of formation for several binary compounds with ab initio simulations and experiments. Due to the high energy of the protons, we described the interaction between the protons and other atoms using the Ziegler-Biersack-Littmark (ZBL) potential [16] during the irradiation simulation process. This ZBL potential includes an additional switching function that connects the ZBL potential and the EAM potential and makes the curvature smoothly to zero between an inner (0.7 Å) and outer (1.5 Å) cutoff. In diffusion simulations, periodic boundary conditions were applied in three directions. And in the cascade simulation, periodic boundary conditions were applied in x and y directions, the z direction used the fix boundary condition. The stress relaxation geometry of the simulated system is optimized using the conjugate gradient descent method firstly. Then, the Number-Pressure-Temperature (NPT) (The pressure is at standard atmospheric pressure) ensemble at 600 ℃ was employed inside the simulation box. The system was simulated for about 400 ps, which was enough to ensure the stability of temperature distribution. Finally, The MSDs of all atoms were recorded during the next 600 ps simulation. The timestep was set to 1 fs in all simulations. The cascade simulation was conducted following equilibration in the NPT ensemble for 400 ps, using the Number-Volume-Temperature (NVT) ensemble at 600 ℃ with a time step of 0.001 fs. All atomic configurations were displayed using the open visualization tool (OVITO) software package [17]. The volume analysis in the simulation process was completed using the V_{oro}++ program[18]. The diffusion rates of all atoms and each type atom can be

calculated by using a linear function and the least-squares fitting method to fit the MSD versus time with reference to Einstein's equation (1) [19]:

$$D = \lim_{t \to \infty} [\frac{1}{6t} < \overrightarrow{[r}(t)]^2 >]\qquad(1)$$

where, $<\overrightarrow{[r}(t)]^2>$ is MSD, $\overrightarrow{r}(t)$ is the displacement as a function of time t. The calculation method of $<\overrightarrow{[r}(t)]^2>$ is as follows:

$$< \overrightarrow{[r}(t)]^2 >= \frac{1}{N} \sum_{i=1}^{N} < \overrightarrow{[r}_i (t+t_0)]^2 - \overrightarrow{[r}_i (t_0)]^2 >$$

3. Results

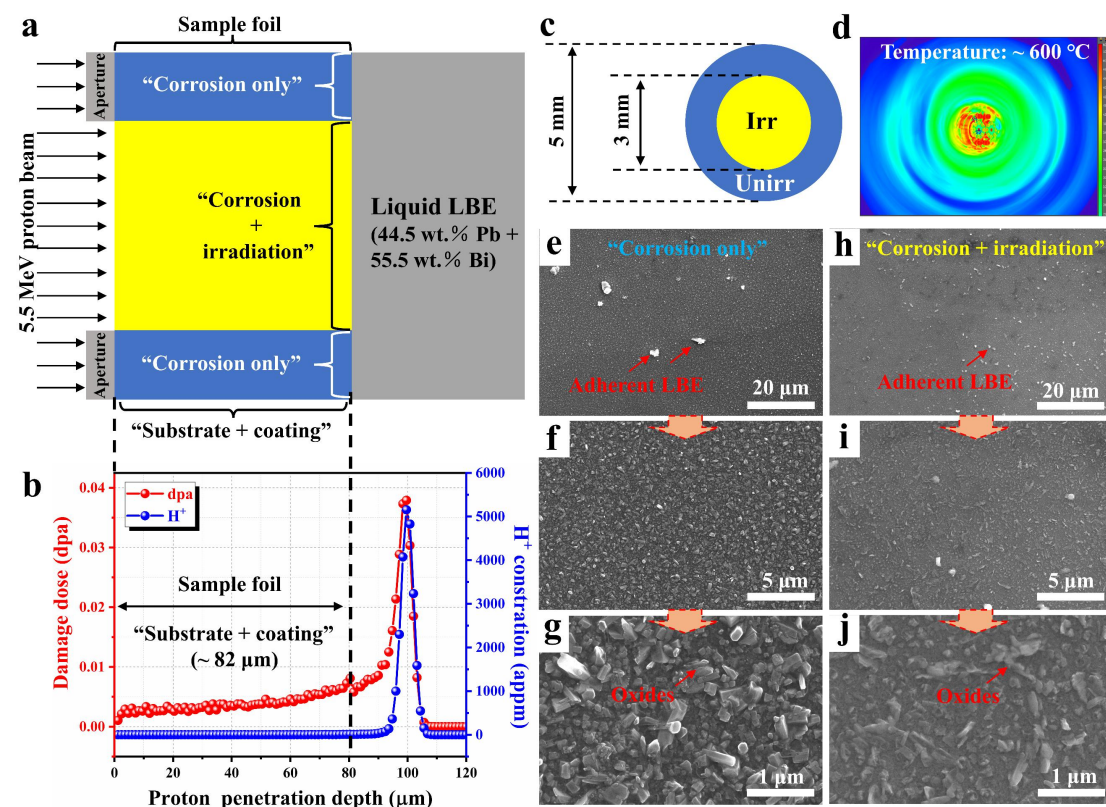## 3.1 Evidence of irradiation-decelerated corrosion of FeCrAlTiMo coatings

Fig. 3. Schematics of the corrosion/irradiation experiment facility, sample configuration, temperature monitoring, and corrosion-facing side comparison areas of FeCrAlTiMo coating: **a** The schematic of corrosion/irradiation experiment facility, showing how the two sample areas of "corrosion only" and "corrosion + irradiation" were created; **b** Distribution of irradiation damage (displacements per atom, dpa) (red dots) and proton deposition concentration (blue dots) along the irradiation direction in sample foil for the FeCrAlTiMo corrosion/irradiation experiment,

simulated by SRIM 2010 [16]; **c** Diagram of shape, size and arrangement of the areas of "corrosion only" (in blue) and "corrosion + irradiation" (in yellow); **d** Infrared thermal imaging of sample temperature; **e-j** Representative SEM images with different resolutions of the corrosion-facing side of the sample foil after 12 h at about 600 ℃ under the average beam current density of 3.48 μA/cm^2; **e-g** and **h-j** correspond to the "corrosion only" and "corrosion + irradiation" areas, respectively.

The thin sample foil (substrate + coating) with a total thickness of about 82 μm (**Fig. 2**) was simultaneously exposed to 600 ℃ liquid LBE (**Fig. 3d**) and proton beams in a previously constructed corrosion/irradiation experiment facility [13]. **Fig. 3a** presented the core diagram of the corrosion/irradiation experiment facility, where two contrasting areas were flexibly obtained, one was the central area that was subjected to both liquid LBE corrosion and proton irradiation, while the other outer area was only exposed to liquid LBE (**Fig. 3c**). According to the SRIM simulation (**Fig. 3b**), the sample foil thickness (82 μm) was far from the Bragg peak position (98 μm) where most protons were deposited, indicating that proton irradiation damage was introduced into the coating without significant hydrogen implantation. Therefore, the effect of hydrogen injection on the corrosion behavior of coating was negligible. The scanning electron microscope (SEM) images with different resolution of the irradiated area and unirradiated area revealed remarkable differences in LBE corrosion behavior between them (**Fig. 3e-j**). The unirradiated area was covered by continuous and dense oxide particles (**Fig. 3g**), while the average size and number density of oxide particles formed in the irradiated area were significantly reduced (**Fig. 3j**), implying irradiation-decelerated corrosion. The proton irradiation, as the only difference between the two areas, was certainly the only reason dedicated to slowing down LBE corrosion rate of coating.

3.2 Quantification of decelerated-corrosion by analyzing oxide film
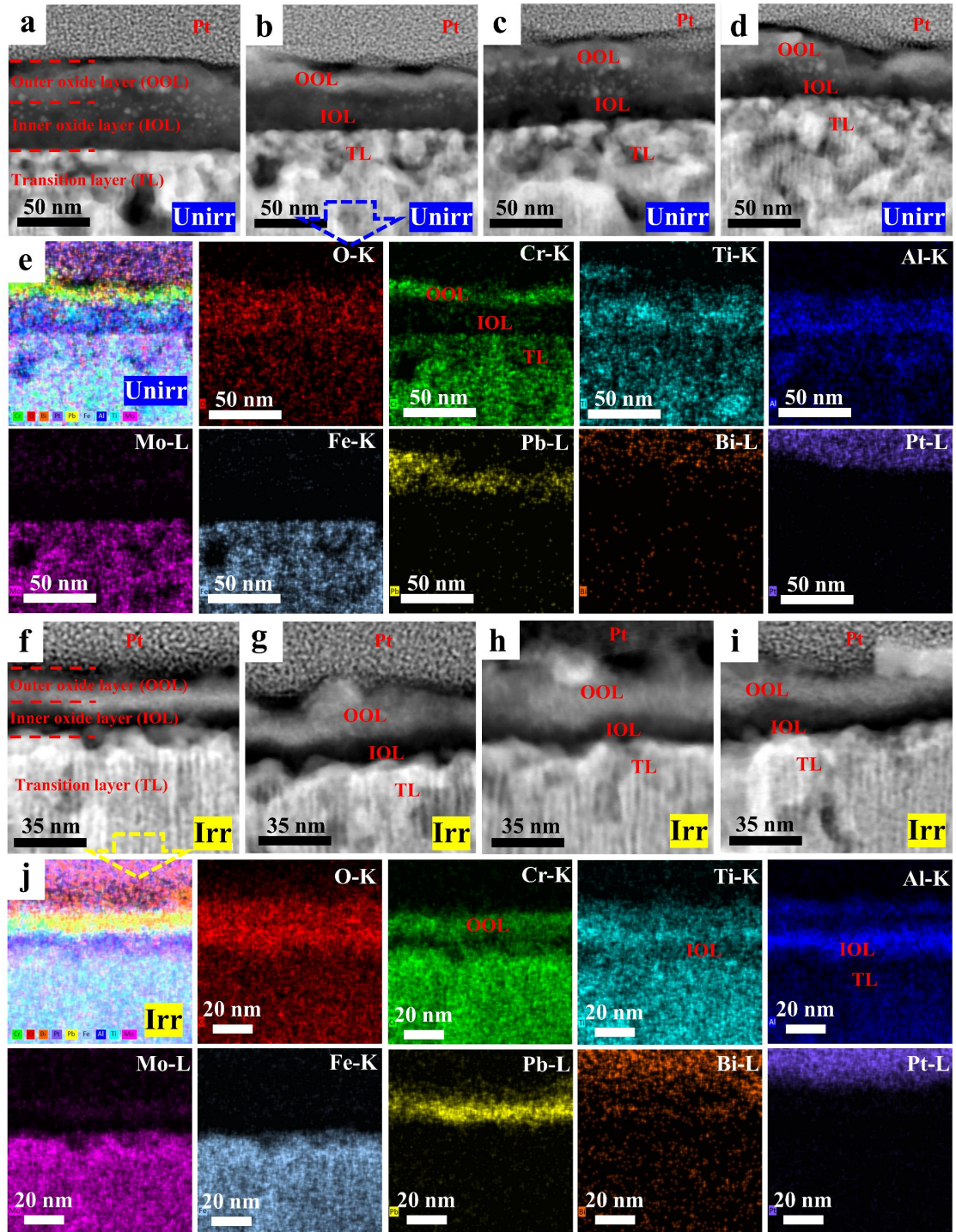

Fig. 4. Cross-sectional TEM analysis of the oxide film formed in the irradiated and unirradiated areas of the exposed FeCrAlTiMo coating for quantitatively comparing the difference in LBE corrosion behavior: **a-d** High-angle annular dark-field (HAADF) TEM images and **e** EDS mapping results of the oxide film formed in unirradiated areas; **f-i** High-angle annular dark-field TEM images and **j** EDS mapping results of the oxide film formed in irradiated areas.

To further confirm the effect of irradiation-decelerated corrosion, **Fig. 4** presented the cross-sectional TEM analysis of the oxide film formed in irradiated and unirradiated areas for quantitatively comparing the difference in LBE corrosion behavior. From the HAADF images (**Fig. 4a-d and f-i**), both the coating surface of irradiated and unirradiated areas was covered by a thin and continuous oxide film, which was mainly characterized by a double-layer structure with an outer oxide layer (OOL) in gray contrast and an inner oxide layer (IOL) in dark contrast. According to the EDS mapping results (**Fig. 4e**), the oxide film formed in the unirradiated areas showed the enrichment of Cr and O at the OOL, while Al, Ti and O were enriched at the IOL, which were eventually identified as the hexagonal Cr_2O_3 OOL and the mixed amorphous Al_2O_3/rutile TiO_2 IOL, as shown in **Fig. 5**. However, in contrast to unirradiated area, where a mixed Al_2O_3/TiO_2 IOL was observed, the irradiated area showed signals from Cr and Ti in the OOL, identifying the hexagonal Cr_2O_3 and rutile TiO_2, and signals from Al at the IOL, identifying the amorphous Al_2O_3 (**Fig. 5**). These results indicated that irradiation promoted the separation of Al_2O_3 and TiO_2. Besides, a transitional area between the oxide film and alloy coating, characterized with the depletion of oxide former (Al, Ti and Cr), was formed after corrosion, which usually called transitional layer (TL). The Al dissipation was more serious than that of Cr and Ti in both irradiated and unirradiated areas (**Fig. 4e and j**). In addition, the dissipation of Al, Ti and Cr in the irradiated area was significantly weaker than that in the unirradiated area, which also implied that irradiation slowed down corrosion.
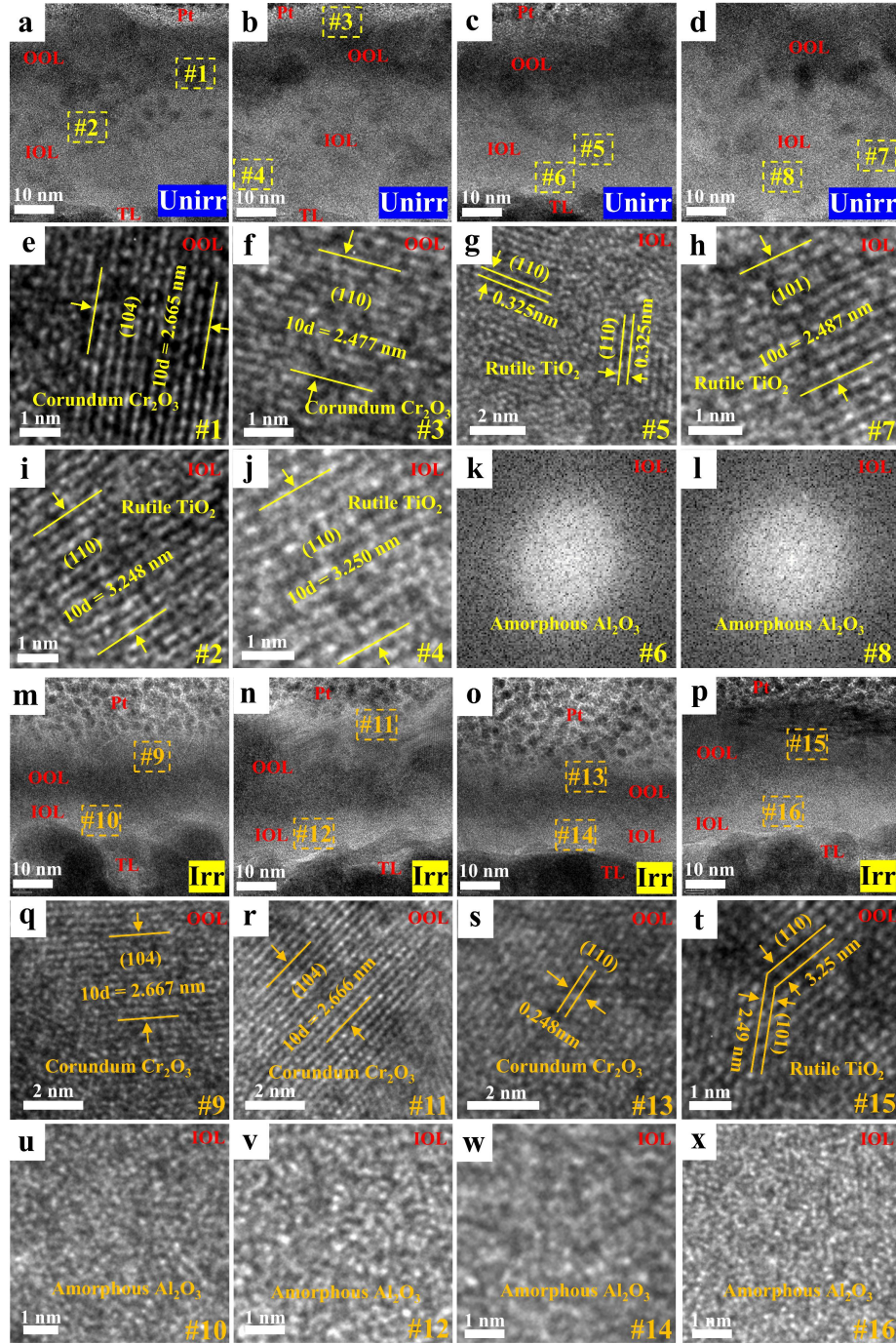
Fig. 5. Microstructure analysis of the oxide film formed in the irradiated and unirradiated areas of the exposed FeCrAlTiMo coating for quantitatively comparing the difference in LBE corrosion behavior: **a-d** Bright-field TEM images of the oxide film formed in the unirradiated area; **e-f** high-resolution (HR) TEM images of the outer oxide layer as marked in corresponding bright-field TEM images **a-d**; **g-j** HRTEM images and **k-l** fast Fourier transform (FFT) patterns of the inner oxide layer as marked in corresponding bright-field TEM images **a-d**; **m-p** Bright-field TEM images of the oxide film formed in the irradiated area; **q-t** high-resolution (HR) TEM images of the outer oxide layer as marked in corresponding bright-field TEM images **m-p**; **u-x** HRTEM images of the inner oxide layer as marked in corresponding bright-field TEM images **m-p**.

To make quantitative comparisons of the difference in corrosion behavior between irradiated and unirradiated areas, we summarized the thickness of the oxide layer and transitional layer from twenty independent HRTEM and HAADF images, as exhibited in **Fig. 6**. Comparing the minimum, maximum and average thickness of the outer oxide layer, inner oxide layer, total oxide layer and transitional layer of the irradiated and unirradiated areas at the same corrosion conditions (time and temperature), corrosion was distinctly weaker in the irradiation area. As shown in **Fig. 6c**, based on the total oxide layer thickness, the unirradiated area was corroded roughly 1.4~1.5 times higher than the irradiated area. To sum up, our experimental results confirmed that in-situ proton irradiation decelerated the LBE corrosion rate of the FeCrAlTiMo coating.
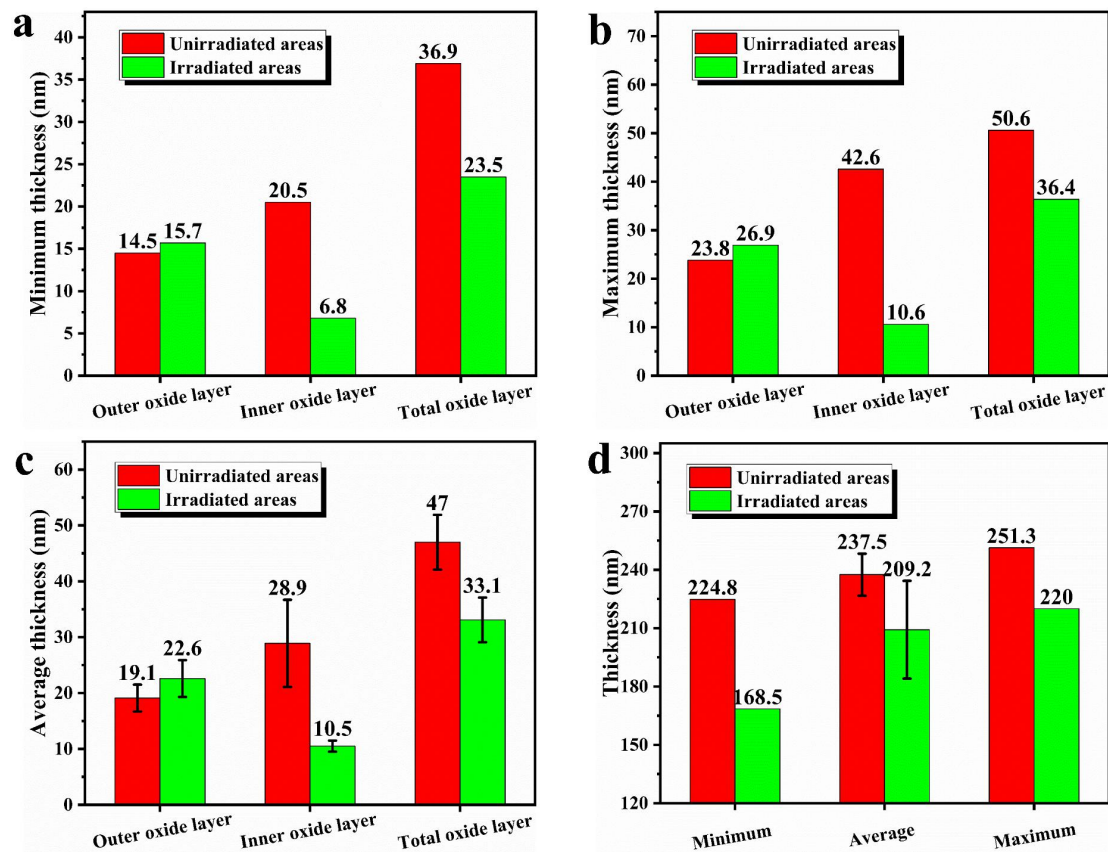

Fig. 6. Quantitative comparison of corrosion behavior in irradiated and unirradiated areas of the FeCrAlTiMo coating: **a** Minimum, **b** maximum and **c** average thickness of the outer oxide layer, inner oxide layer and total oxide layer; **d** Minimum, maximum and average thickness of the transitional layer.

4. Discussion

4.1 Mechanism analysis of proton-decelerated corrosion
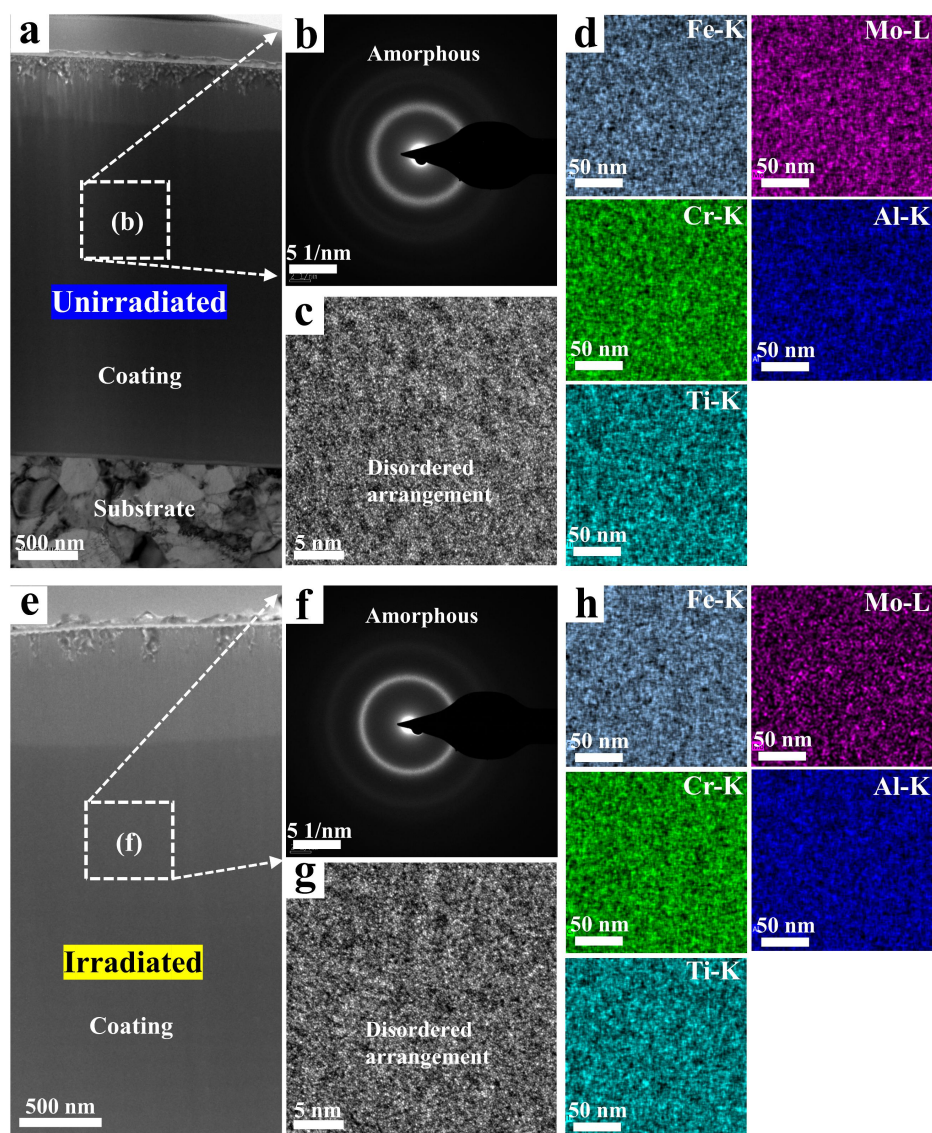

Fig. 7. Microstructure analysis of the exposed FeCrAlTiMo coating corresponding to the irradiated and unirradiated areas: **a** cross-sectional TEM image, **b** SAED pattern, **c** HRTEM image and **d** EDS mapping of the unirradiated area; **e** cross-sectional TEM image, **f** SAED pattern, **g** HRTEM image and **h** EDS mapping of the irradiated area.

Under the condition of saturated oxygen, the LBE corrosion on coating appeared as oxidation (**Fig. 4**). The irradiation had little effect on the double-layer structure and phase composition (Cr_2O_3, TiO_2 and Al_2O_3) of the oxide film formed on the exposed coating (**Fig. 5** and **Fig. 6**), which meant that irradiation retarded corrosion (**Fig. 6**)

primarily by affecting corrosion kinetics rather than thermodynamics, suggesting that there was a mechanism by which irradiation reduced the diffusion kinetics of coating elements in this study.

However, the irradiation effects on corrosion always appeared to be accelerated [4, 20-22], which was attributed to irradiation-induced structural defects (dislocation loops, voids, bubbles, etc.) and spatial redistribution of chemical components (precipitates and segregation). The energetic incident particles dislocated the target atoms in a cascaded way, inevitably resulting in vacancies, interstitials and other irradiation defects evolved from them. These defects provided fast pathways for the movement of atoms and increased the diffusion rate of certain elements in the materials, thus accelerating the corrosion [9]. As shown in **Fig. 7**, the amorphous structure of the FeCrAlTiMo coating still maintained after exposure to high-temperature/LBE/irradiation multi-field environment, and no discernable precipitation and segregation were detected, indicating good structural stability. It was well established that amorphous metallic glasses differed from traditional crystalline materials in their unique structural feature of long-range disorder and short-range order, which marked them free of crystalline defects such as dislocation lines/loops/walls, etc. [23]. Owing to the stable amorphous nature and no crystalline defects, the contribution strength of typical irradiation-induced defects to enhanced corrosion was greatly weakened in this study.
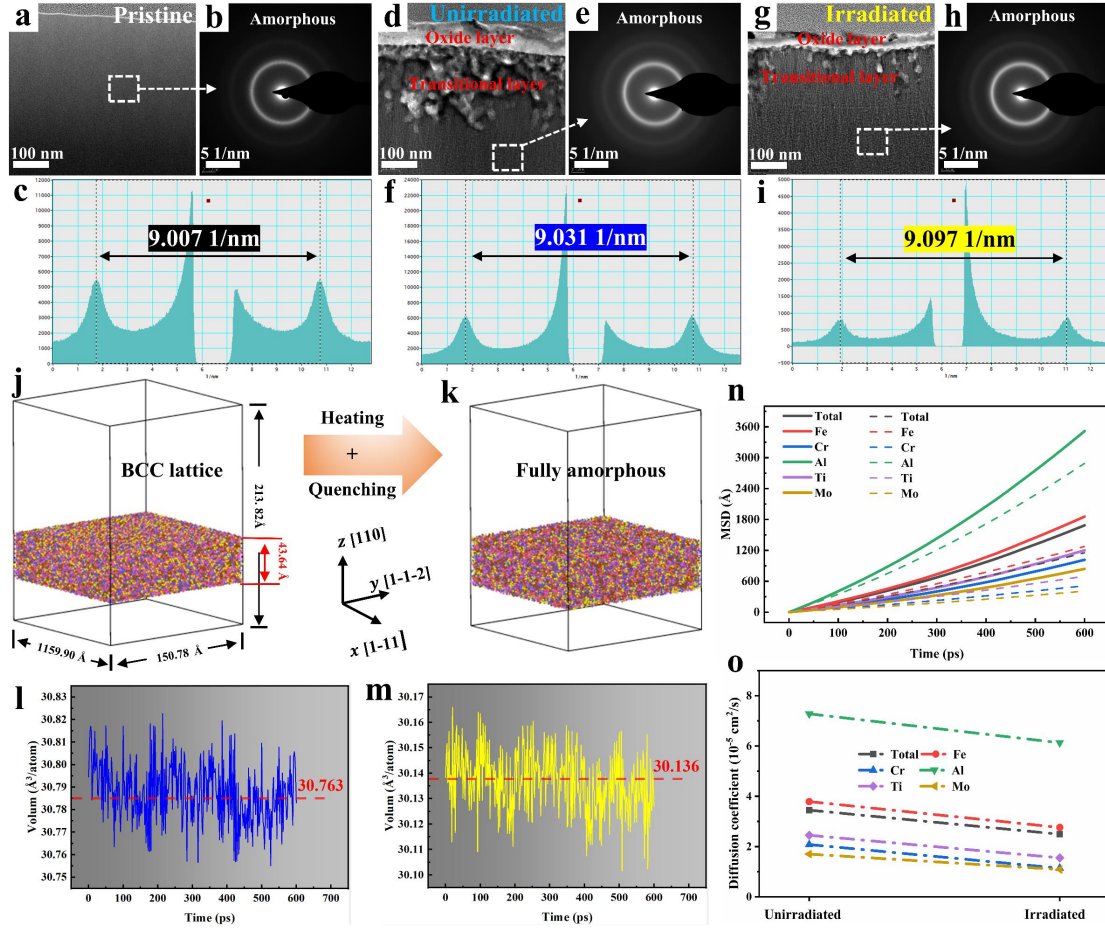
Fig. 8. The evolution of the coating free volume and the comparative analysis of diffusion coefficients of coating elements: **a** TEM image, **b** SAED pattern and **c** diameter measurement of diffraction halo of the pristine coating; **d** TEM image, **e** SAED pattern and **f** diameter measurement of diffraction halo of the unirradiated coating; **g** TEM image, **h** SAED pattern and **i** diameter measurement of diffraction halo of the irradiated coating; **j** and **k** Molecular dynamics modeling process of amorphous structure of the FeCrAlTiMo coating; The evolution of the average volume per atom in amorphous FCATM' (110) with time before **l** and after **m** irradiation; **n** MSD versus time curves for FCATM' (110), where the solid line represents the results before irradiation, while the dashed line represents the results after irradiation; **o** Comparison of atomic diffusion coefficients of elements in FCATM' (110) before and after irradiation.

Building on previous work, it was generally perceived that metallic glasses mainly consisted of tightly bonded atomic clusters that overlapped and formed the percolating 'skeleton' of the glassy structure, with loosely bounded free-volume regions embedded within it [24]. Analogous to crystalline materials, these free-volume regions were treated as typical structural defects inside metallic glasses, and it was widely demonstrated that an increase in the free volume fraction leaded to a significant increase in the diffusion coefficient [25, 26]. In fact, from the SAED

patterns (**Fig. 8b, e and h**), some subtle difference could still be observed in the pristine, irradiated and unirradiated coatings. The diameters of diffraction halos of the pristine, unirradiated and irradiated coatings were 9.007 1/nm, 9.031 1/nm and 9.097 1/nm, respectively (**Fig. 8c, f and i**), indicating that the average interatomic distance became smaller and the arrangement of atoms became tighter. In other words, the equivalent high-temperature annealing and irradiation promoted the free volume to annihilate, thus reducing the free volume fraction, as reported in other studies [27, 28]. Since the unirradiated and irradiated coatings underwent the same thermal aging, the thermal effect would not be discussed here and only irradiation effect were focused on.

Considering the possible inaccuracies of the experimental measurements, the response of the coating volume to proton irradiation and the accompanying variation of the element diffusion coefficient were further calculated by molecular dynamics (MD) simulation. **Fig. 8l and m** showed the evolution of the average volume per atom (V_p) over time for the unirradiated and irradiated coatings, respectively, with a total time of 600 ps. Averaging the V_p over the recorded time to get the V_{ap}, the V_{ap} of the irradiated coating (30.136 $Å^3$/atom) was less than that of the unirradiated coating (30.763 $Å^3$/atom), indicating that the free volume in the coating was reduced after irradiation, which was consistent with the results of SAED patterns (**Fig. 8c, f and i**). **Fig. 8n** represented the change of MSD (mean square displacement) of each atom in the irradiated (dotted line) and unirradiated (solid line) coatings over recorded time. The slope of MSD versus time curve of the irradiated coating was significantly lower than that of the unirradiated coating, implying a smaller diffusion rate. According to the Einstein's equation [19], the calculated diffusion coefficients of the unirradiated and irradiated coatings were plotted in **Fig. 8o**. It was evident that the diffusion coefficients of the total and each atom were reduced after irradiation. Lower diffusion coefficient meant slower diffusion kinetics, which reasonably explained the decelerated LBE corrosion rate of irradiated coatings, i.e. thinner oxide film and transitional layer (**Fig. 3**).

Based on the above analysis, a mechanism considering irradiation-reduced diffusion was proposed to explain how irradiation enhanced the corrosion resistance

of materials. In our study, the FeCrAlTiMo coating retained amorphous structure after simultaneous irradiation and corrosion. The interstitial-like and vacancy-like point defects generated by irradiation damage cascades were transient, unstable, and completely annihilated, and could not evolve into large-size structural defects such as dislocations [29]. On the contrary, the irradiation-induced thermal peaks and viscous flow resulted in the annihilation and redistribution of the free volume [27, 30], reducing the diffusion kinetics of the coating and leading to decelerated corrosion, which challenged the traditional wisdom that irradiation accelerated corrosion. This abnormal mechanism of irradiation-decelerated corrosion was hypothesized to be generally effective in an amorphous alloy, independent of the type of corrosive medium. Therefore, this effect can be adopted to design new amorphous nuclear structural materials with high phase structural stability to achieve better synergistic corrosion and irradiation resistance, which has important implications for the design and rapid development of structural materials, and finally usher in future advanced nuclear energy systems.

Conclusions

Synergistic effect of the simultaneous proton irradiation and LBE corrosion on FeCrAlTiMo coating was investigated. The surface morphology, elementary composition, microstructure and crystal structure of the oxide scale were systematically analyzed. The following conclusions can be drawn:

(1) The composition and crystal structure of the oxide scale formed on the FeCrAlTiMo coating after exposure to 600 ℃ molten LBE were nearly not affected by proton irradiation. The oxide scale of the irradiated and unirradiated areas consisted of a Cr_2O_3 outer layer and a mixed TiO_2/Al_2O_3 inner layer. Noted that irradiation could promote the separation of Al_2O_3 and TiO_2.

(2) Proton irradiation decelerated the LBE corrosion of the FeCrAlTiMo coating. The thicknesses of the inner and total oxide layers decreased obviously, but the outer layer increased slightly after irradiation.

(3) Proton irradiation-decelerated corrosion could be attributed to irradiation-induced annihilation and redistribution of the free volume, which reduced the diffusion kinetics of the coating elements and lead to slower corrosion.

Acknowledgements

Data availability

All data generated or analyzed during this study are included in the published article and its supplementary information files.

References

[1] J.E. Kelly, Generation IV International Forum: A decade of progress through international cooperation, Progress in Nuclear Energy, 77 (2014) 240-246.

[2] X. Gong, M.P. Short, T. Auger, E. Charalampopoulou, K. Lambrinou, Environmental degradation of structural materials in liquid lead- and lead-bismuth eutectic-cooled reactors, Progress in Materials Science, 126 (2022) 100920.

[3] H. Zhu, R. Holmes, T. Hanley, J. Davis, K. Short, L. Edwards, Z. Li, Effects of bubbles on high-temperature corrosion of helium ion-irradiated Ni-based alloy in fluoride molten salt, Corrosion Science, 125 (2017) 184-193.

[4] P. Deng, Q. Peng, E.-H. Han, W. Ke, C. Sun, Z. Jiao, Effect of irradiation on corrosion of 304 nuclear grade stainless steel in simulated PWR primary water, Corrosion Science, 127 (2017) 91-100.

[5] Q. Chen, F. Bai, P. Wang, J. Yang, C. Zhu, W. Zhang, H. Liu, Y. Zhong, J. Deng, N. Liu, J. Yang, Microstructure response and lead-bismuth eutectic corrosion behavior of 11Cr1Si ferritic/martensitic steel after Au-ion irradiation, Corrosion Science, 198 (2022) 110101.

[6] G. Lei, S. Yang, H. Huang, Q. Huang, R. Liu, W. Zhang, G. Yu, L. Yan, Corrosion-driven outward migration and growth of helium bubbles in a nickel-based alloy in high-temperature molten salt environment, Corrosion Science, 153 (2019) 47-52.

[7] R. Wang, P. Li, B. Li, L. Hu, F. Huang, Q. Huang, F. Ge, The oxidation mechanisms of the Xe20+ ion-irradiated Cr coatings on Zr alloy coupons: Accelerated diffusion and internal oxidation, Corrosion Science, 201 (2022) 110301.

[8] X. Guo, S. Cong, Z. Liu, L. Zhang, Z. Ma, Z. Zhou, M. Song, J. Yang, Irradiation accelerated corrosion of alumina-forming austenitic steels in supercritical CO2: The oxide scale formed within an individual grain or affected by grain boundary, Corrosion Science, 221 (2023) 111207.

[9] Z. Cheng, J. Sun, X. Gao, Y. Wang, J. Cui, T. Wang, H. Chang, Irradiation effects in high-entropy alloys and their applications, Journal of Alloys and Compounds, 930 (2023) 166768.

[10] Z. Zhu, H. Huang, G. Lei, Y. Wu, C. Ren, A. Liu, Z. Zhu, Synergistic effect of irradiation and molten salt corrosion: Acceleration or deceleration?, Corrosion Science, 185 (2021) 109434.

[11] W. Zhou, Y. Yang, G. Zheng, K.B. Woller, P.W. Stahle, A.M. Minor, M.P. Short, Proton irradiation-decelerated intergranular corrosion of Ni-Cr alloys in molten salt, Nat Commun, 11 (2020) 3430.

[12] J. Yang, F. Zhang, Q. Chen, W. Zhang, C. Zhu, J. Deng, Y. Zhong, J. Liao, Y. Yang, N. Liu, J. Yang, Effect of Au-ions irradiation on mechanical and LBE corrosion properties of amorphous AlCrFeMoTi HEA coating: Enhanced or deteriorated?, Corrosion Science, 192 (2021) 109862.

[13] Q. Chen, Y. Chen, F. Zhang, J. Yang, C. Zhu, W. Zhang, H. Liu, Y. Zhong, J. Deng, Q. Li, N. Liu, J. Yang, In-situ proton irradiation/lead-bismuth eutectic corrosion synergistic effect on corrosion behaviour of 11Cr1W1Si ferritic/martensitic steel,

Journal of Nuclear Materials, 573 (2023) 154097.

[14] P. Steve, Fast Parallel Algorithms for Short-Range Molecular Dynamics, Journal of computational physics, 117 (1995) 1-19.

[15] X.W. Zhou, R.A. Johnson, H.N.G. Wadley, Misfit-energy-increasing dislocations in vapor-deposited CoFe/NiFe multilayers, Physical Review B, 69 (2004) 144113.

[16] J.F. Ziegler, M.D. Ziegler, J.P. Biersack, SRIM–The stopping and range of ions in matter (2010), Nuclear Instruments and Methods in Physics Research Section B: Beam Interactions with Materials and Atoms, 268 (2010) 1818-1823.

[17] A. Stukowski, Visualization and analysis of atomistic simulation data with OVITO–the Open Visualization Tool, Modelling and Simulation in Materials Science and Engineering, 18 (2010) 015012.

[18] C.H. Rycroft, VORO^{++}: A three-dimensional Voronoi cell library in C^{++}, Chaos: An Interdisciplinary Journal of Nonlinear Science, 19 (2009) 041111.

[19] M.A. Kovalenko, A.Y. Kupryazhkin, Mechanisms of exchange and anion frenkel diffusion in uranium dioxide: Molecular dynamics study, Journal of Nuclear Materials, 522 (2019) 255-264.

[20] J. Li, H. Huang, Q. Huang, M. Tang, B. Zhao, G. Ji, W. Zhang, R. Xie, L. Yan, Effect of irradiation damage on corrosion of 4H-SiC in FLiNaK molten salt, Corrosion Science, 125 (2017) 194-197.

[21] M. Boisson, L. Legras, E. Andrieu, L. Laffont, Role of irradiation and irradiation defects on the oxidation first stages of a 316L austenitic stainless steel, Corrosion Science, 161 (2019) 108194.

[22] X. Lin, Q. Peng, J. Mei, E.-H. Han, W. Ke, L. Qiao, Z. Jiao, Corrosion of phase and phase boundary in proton-irradiated 308L stainless steel weld metal in simulated PWR primary water, Corrosion Science, 165 (2020) 108401.

[23] Y.Q. Cheng, E. Ma, Atomic-level structure and structure–property relationship in metallic glasses, Progress in Materials Science, 56 (2011) 379-473.

[24] J.C. Ye, J. Lu, C.T. Liu, Q. Wang, Y. Yang, Atomistic free-volume zones and inelastic deformation of metallic glasses, Nature Materials, 9 (2010) 619-623.

[25] D. Klaumünzer, A. Lazarev, R. Maaß, F.H. Dalla Torre, A. Vinogradov, J.F. Löffler, Probing Shear-Band Initiation in Metallic Glasses, Physical Review Letters, 107 (2011) 185502.

[26] K. Wang, T. Fujita, Y.Q. Zeng, N. Nishiyama, A. Inoue, M.W. Chen, Micromechanisms of serrated flow in a Ni50Pd30P20 bulk metallic glass with a large compression plasticity, Acta Materialia, 56 (2008) 2834-2842.

[27] J. Yang, K. Shi, Q. Chen, W. Zhang, C. Zhu, Z. Ning, J. Liao, Y. Yang, N. Liu, W. Zhang, J. Yang, Effect of Au-ion irradiation on the surface morphology, microstructure and mechanical properties of amorphous AlCrFeMoTi HEA coating, Surface and Coatings Technology, 418 (2021) 127252.

[28] J. Gu, M. Song, S. Ni, S. Guo, Y. He, Effects of annealing on the hardness and elastic modulus of a $Cu_{36}Zr_{48}Al_8Ag_8$ bulk metallic glass, Materials & Design, 47 (2013) 706-710.

[29] Y.F. Wang, H.Y. Li, L. Yang, Radiation-induced structural evolution in Zr_2Cu metallic glass, Journal of Materials Science, 53 (2018) 10979-10986.

[30] X.L. Bian, G. Wang, H.C. Chen, L. Yan, J.G. Wang, Q. Wang, P.F. Hu, J.L. Ren, K.C. Chan, N. Zheng, A. Teresiak, Y.L. Gao, Q.J. Zhai, J. Eckert, J. Beadsworth, K.A. Dahmen, P.K. Liaw, Manipulation of free volumes in a metallic glass through Xe-ion irradiation, Acta Materialia, 106 (2016) 66-77.